Electronic Supplementary Material (ESI) for Journal of Materials Chemistry A.

Supporting information

Improved interfacial chemistry and enhanced high voltage-resistant capability of in-situ polymerized electrolyte for $LiNi_{0.8}Co_{0.15}Al_{0.05}O_2$-Li batteries

Yue Ma[1], Qifang Sun[1], Zhenyu Wang[2], Su Wang[1], Ying Zhou[1], Dawei Song[1], Hongzhou Zhang[1, *], Xixi Shi[1], Chunliang Li[1], Lianqi Zhang[1, *] and Lingyun Zhu[2]

Experimental section

Materials

Lithium foil was purchased from (China Energy Lithium Co., Ltd) and transferred to glove box for further use. $LiNi_{0.8}Co_{0.15}Al_{0.05}O_2$ (self-prepared by our group), $LiFePO_4$ (Tianjin EV Energies Co., Ltd) and acetylene black (Sigma-Aldrich Inc.) were used after drying in the oven at 120 ℃ for 12 h. PVDF (5130) binder, Maleic anhydride (MA) and methyl methacrylate (MMA) were purchased from Sigma-Aldrich Inc., MA and MMA should be stored under cool condition. Hexafluorobutyl methacrylate (HFMA) was purchased from Meryer and stored at 8-10 °C.

Preparation of in-situ PMHM electrolyte and LMBs

Firstly, HFMA and MA (in weight ratio of 1:1) were dissolved into 1 ml liquid electrolyte consist of 1M $LiFP_6$ in EC/DMC (1:1, v:v). The mixture was fully stirred at room temperature for 1 h. Then MMA monomer with the same content as HFMA was added in the above mixture and stirred for another 1h. Afterwards, the thermal initiator azodiisobutyronitrile (AIBN) with the content of 5 wt.% and 1 wt.% of FEC were added into the above solution and stirred for 0.5 h to obtain homogenous precursor. The solid content of the in-situ gel polymer precursor was 30 wt.%.

$LiFePO_4$ (LFP)/$LiNi_{0.8}Co_{0.15}Al_{0.05}O_2$ (NCA) cathode composed of 80 wt.% LFP/NCA, 10 wt.% Super P, 10 wt.% PVDF with the areal density about 1.8 mg cm^{-2} was prepared. Lithium foil was taken as anode. The electrolyte precursor with the volume of 60 ul was injected into 2032-type coin cell, cellulose membrane was applied as the supporting matrix to prevent short circuits of PMHM. The resultant battery was kept on heating stage at 40°C for 4 h and 60°C for 6 h to achieve poly(maleic anhydride-hexafluorobutyl methacrylate-methyl methacrylate) (abbreviated as PMHM) electrolyte.

Characterization

Fourier transform infrared spectrometers (FT-IR, Frontier Mid-IR FTIR) was conducted to investigate the molecular structure of PMHM and the molecular weight is monitored with Gel permeation chromatography (GPC, Agilent PL-GPC50). Scanning electron microscopy (SEM, Quanta FEG 250) was carried out to observe the morphology and the thickness of PMHM electrolyte as well as the electrodes morphology variation during cycling. Transmission electron microscopy (TEM, JEM2100PLUS) was performed to characterize the morphology of cathode electrolyte interphase formed on cathode. X-ray diffraction (XRD, Ultima IV) was conducted to evaluate the crystallinity degree of PMHM and to investigate the electrode structure variation during cycling. X-ray photoelectron spectroscopy (XPS, Thermo Escalab 250) was applied to analyze the composition of cathode electrolyte interphase and solid electrolyte interphase. Thermogravimetric analysis (TG) test was also performed with STA449F5. Nuclear magnetic resonance (NMR) spectra were acquired using a Brucker AVANCE Ⅲ HD400 MHz. The data were analyzed with the MestReNova software. The static state contact angle test was conducted by contact angle meter (JY-82B Kruss DSA). Atomic force microscopy (AFM) was used to test the Young modulus of electrolyte (NT-MDT Prima).

Electrochemical test

Ionic conductivity (σ) of PMHM was measured in a block stainless steel (SS)/PMHM/SS symmetrical cell via electrochemical impedance spectroscopy (EIS) according to the following equation (1):

$$\sigma = d/RS \quad (1)$$

Where d (cm) is the thickness of PMHM, S (cm^{-2}) belongs to the effective area of PMHM, while R represents the bulk resistance of PMHM. EIS was conducted in the frequency range from 1MHz to 100 mHz through multi-channel electrochemical workstation (PARSTAT). The Vogel-Tamman-Fulcher (VTF) empirical equation is listed as follows:

$$\sigma = AT^{1/2} exp[\frac{-Ea}{R(T-T_0)}] \quad (2)$$

where A is the pre-exponential factor, Ea is the activation energy, R is the ideal gas constant and T_0 is a parameter related to the glass transition temperature. Electrochemical stability window of electrolyte was tested via linear sweep voltammetry (LSV) using Li/PMHM/SS unsymmetrical cell in the potential range from 0 to 6 V vs. Li^+/Li. Lithium ion transfer number (t_{Li^+}) was measured via a conventional electrochemical method with Li/PMHM/Li symmetrical cell according to the following equation:

$$t_{Li+}=I_s(\Delta V- I_0R_0)/I_0(\Delta V- I_sR_s) \quad (3)$$

Where I_0 and I_s represent the current value of initial and steady-state in DC polarization, while R_0 and R_s stand for the resistance at initial and steady-state in AC impedance test. ΔV is the potential amplitude of 10 mV. Li/PMHM/Li symmetrical cells were also performed to investigate the lithium stripping/plating behavior. Cycling performance and rate performance of LFP/PMHM/Li and NCA/PMHM/Li batteries were investigated in the potential range of 2.7-4.0 V and 3.0-4.3 V using LAND testing system (Wuhan LAND electronics Co., Ltd.), respectively. The C rates in all the electrochemical measurements are defined based on 1C =170 mA g^{-1} for LFP and 1C =200 mA g^{-1} for NCA. The battery was assembled in an argon-filled glove box with O_2 and H_2O content of below 0.1 ppm.

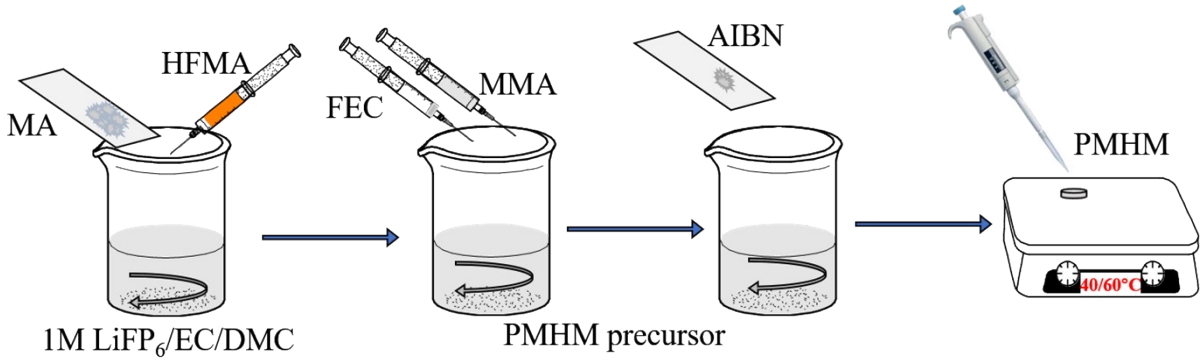

Fig. S1 Schematic diagram for the preparation process of PMHM.

Fig. S2 Digital image of polymerization of MMA, HFMA, MA to form PMHM.

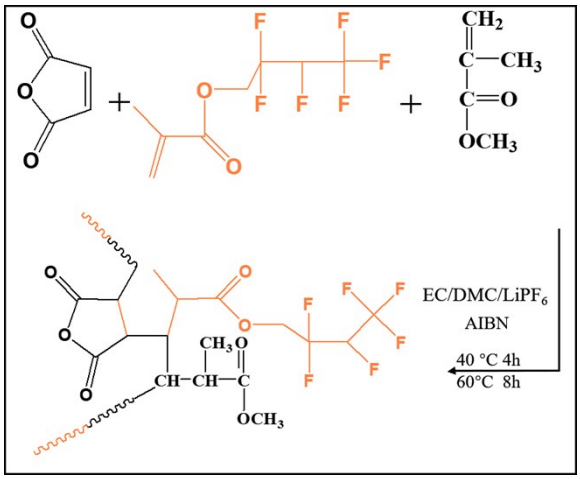

Fig. S3 One of the probable molecular structures of PMHM.

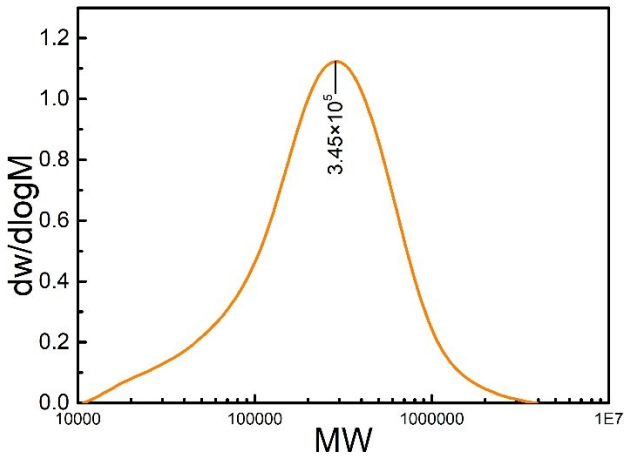

Fig. S4 GPC profile of PMHM.

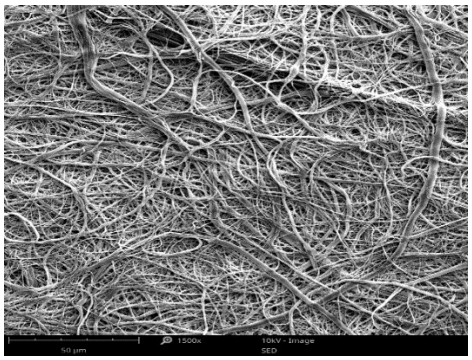

Fig. S5 Typical SEM image of cellulose separator.

Typical SEM image of cellulose separator is shown in **Fig. S5.** It can be seen that uneven fibers with the diameter of 0.2-5 μm are randomly distributed, providing robust skeleton for in-situ PMHM electrolyte.

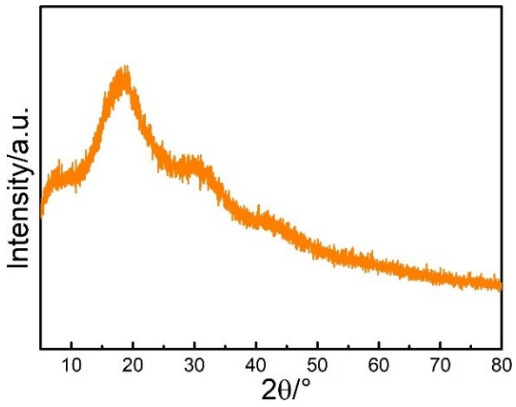

Fig. S6 XRD pattern of PMHM.

XRD pattern is tested from 0 to 80° for the investigation of crystallinity of PMHM and displayed in **Fig. S6**. A bread peak for amorphous phase can be observed at 20°, indicating a flexible motion of molecular chain in PMHM electrolyte.

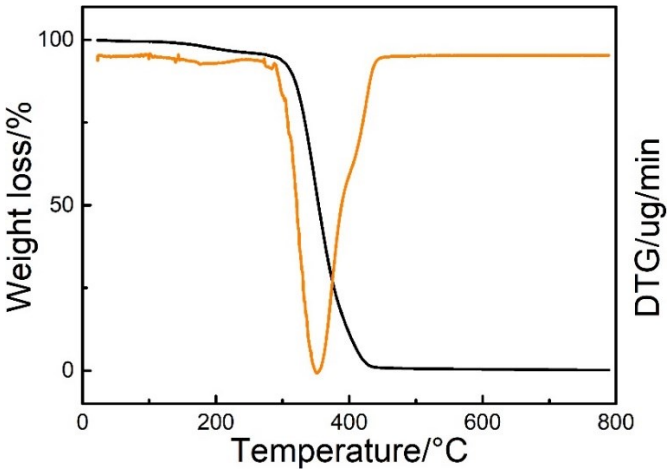

Fig. S7 TG profiles of PMHM.

Thermal stability of PMHM is tested by thermogravimetric analysis and the result is shown in **Fig. S7**. There is no obvious weight loss until 345°C, suggesting the superior thermal stability of PMHM.

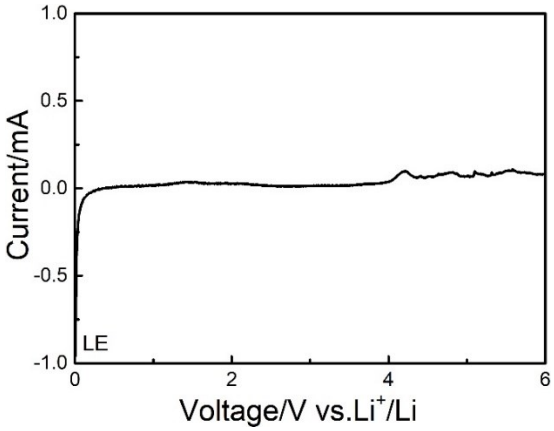

Fig. S8 LSV profile of LE.

Linear sweep voltammetry profile of LE is displayed in **Fig. S8**. It can be seen that the decomposition potentials of LE is 4.1 V, much lower than that of PMHM electrolyte (5.5 V). The significantly improved electrochemical stability of PMHM is attributed to the high voltage resistant advantage of acid anhydride and C-F groups.

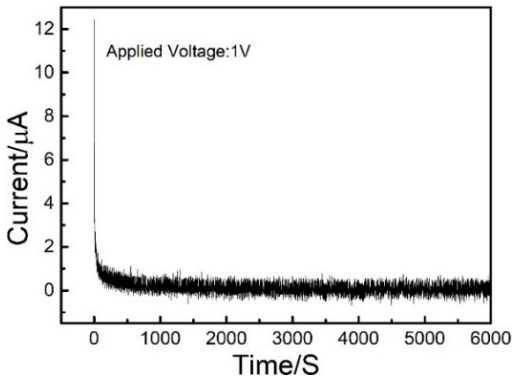

Fig. S9 The time dependent DC current of SS/PMHM/SS under a constant voltage of 1 V.

For solid electrolyte, high ionic conductivity indicates the rapid transfer of Li ions, while large electronic conductivity is probably the root cause for the formation of lithium dendrite when the potential reaches Li-plating potential.[1] The frequency dependent ionic conductivity is measured by AC impedance spectrum using stainless steel/electrolyte/stainless steel symmetrical cell. The electronic conductivity of polymer electrolyte can be investigated via examining the voltage response to a direct current on the cells with the electrolyte sandwiched between two stainless steel blocking electrodes according to the following equation.[2]

$$\gamma = I_s \times l / S \times U \quad (4)$$

where I_s is the steady-state current (34 μA), l is the thickness of solid electrolyte (150 μm), S is the area of electrolyte (Φ = 16.5 mm). By applying a constant voltage (1V), the current first decreases and then reaches a steady state. At the steady state, the current is originated from the electronic leakage since two ion-blocking stainless steel electrodes are used. It should be noted that the electronic conductivity measurement using two ion-blocking electrodes provides an upper limit of the electronic conductivity [3] and the electronic conductivity of PMHM is 25.6×10^{-10} S cm^{-1}.

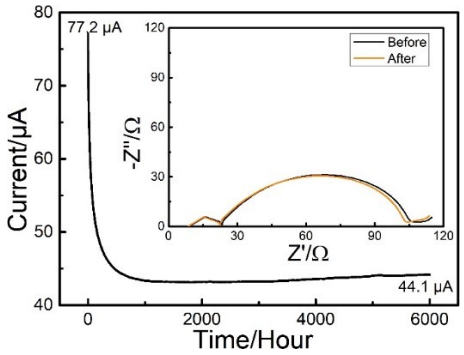

Fig. S10 Current-time profile following a DC polarization of 10 mV for Li/LE/Li symmetrical cell, the insert displays the Nyquist profiles of electrochemical impedance spectroscopy before and after polarization.

Fig. S10 presents the time current profile of Li/LE/Li symmetric cell following a direct current (DC) polarization for 6000 s with the amplitude potential of 0.01 V. The initial current is 77.2 μA and stabilizes at 44.1 μA after polarization, while the corresponding interfacial impedance increases from 103 to 107 Ω. The t_{Li+} of LE is 0.21, which is consistent with the transfer number reported in previous literature and much lower than that of PMHM (0.47).

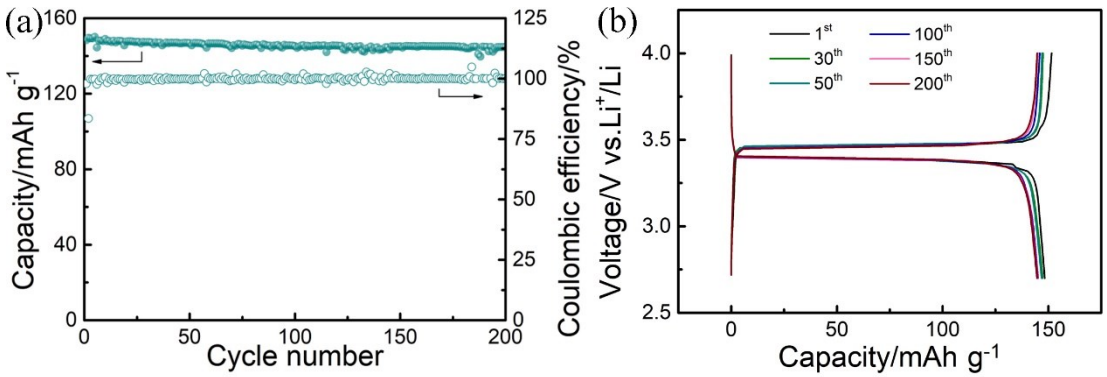

Fig. S11 (a) Cycling performance and (b) galvanostatic charge/discharge profiles of LFP/PMHM/Li batteries at 0.1C.

Fig. S11a exhibits the cycling performance of LFP/PMHM/Li batteries at 0.1C between 2.7 and 4.0 V. The initial discharge capacity is 150 mAh g^{-1}, and a capacity retention of 96.4% is obtained after 200 cycles. **Fig. S11b** shows the charge/discharge profiles of LFP/PMHM/Li batteries during cycling. A very smooth charge/discharge profiles and negligible potential variation can be observed, implying that PMHM is conducive to the transfer of Li ions.

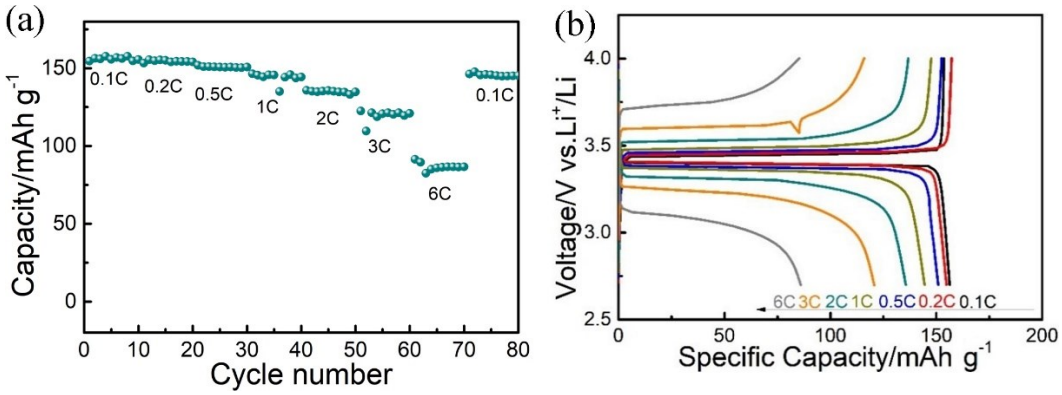

Fig. S12 (a) Rate capability and (b) galvanostatic charge/discharge profiles of LFP/PMHM/Li batteries at various rates.

The discharge capacities at various rates (0.1, 0.2, 0.5, 1, 2, 3 and 6C) are displayed in **Fig. S12**. Specifically, the discharge capacity decreases with the increasing rate, while the polarization increases with the increasing rate. LFP/PMHM/Li battery still delivers a capacity of 150 mAh g^{-1} when the rate returns back 0.1C.

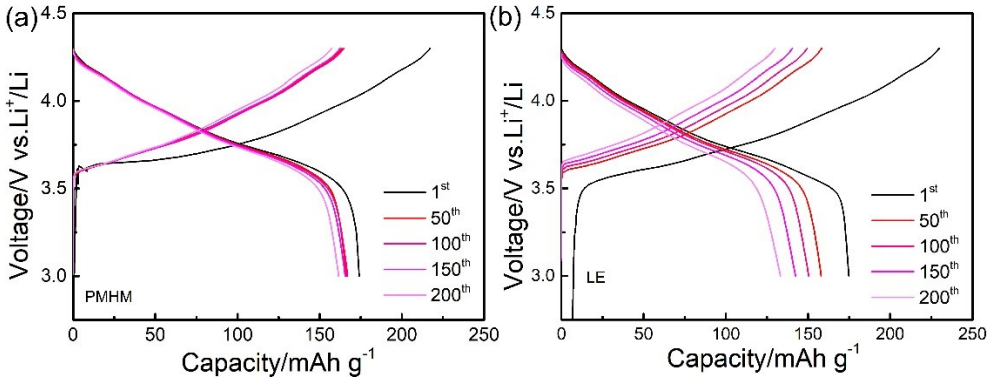

Fig. S13 Galvanostatic charge/discharge profiles of (a) NCA/PMHM/Li and (b) NCA/LE/Li batteries at 0.5C.

Comparison of charge/discharge profiles of NCA/PMHM/Li and NCA/LE/Li batteries are shown in **Fig. S13**. NCA/LE/Li battery presents apparent polarization increase and rapid capacity decay during 200 cycles, which may be attributed to the sluggish intercalation/de-intercalation of Li ions through the electrode/electrolyte interface. As a sharp contrast, superior cycling performance is presented for NCA/PMHM/Li battery, demonstrating the suppressed adverse reactions of electrolyte and the formation of favorable electrode/electrolyte interface.

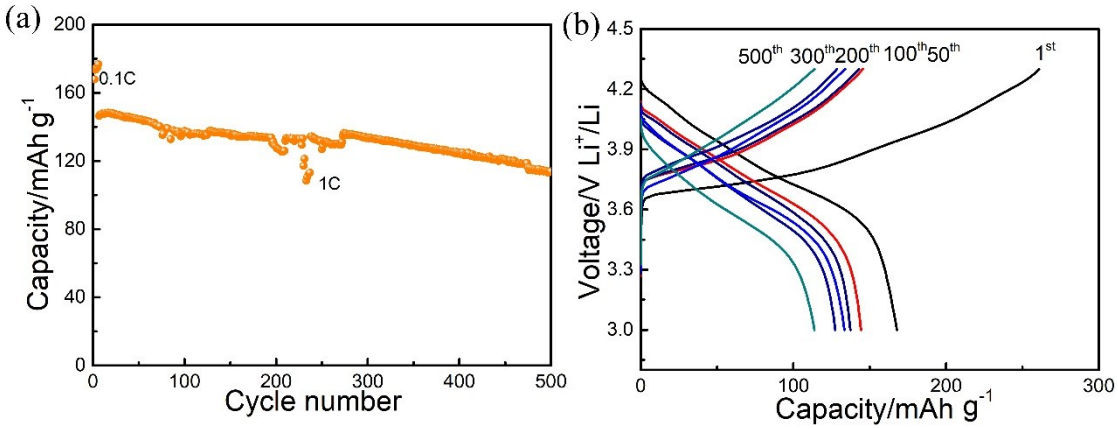

Fig. S14 Cycling performance and galvanostatic charge/discharge profiles of NCA/PMHM/Li battery at 1C.

Fig. S14 displays the cycling performance and galvanostatic charge/discharge profiles of NCA/PMHM/Li battery at 1C for 500 cycles. After the activation process at 0.1C in the initial 10 cycles, a discharge capacity of 113.8 $mAhg^{-1}$ and the capacity retention of 76.7% (the ratio of the final value to the highest capacity at 1C) is delivered after 500 cycle at 1C.

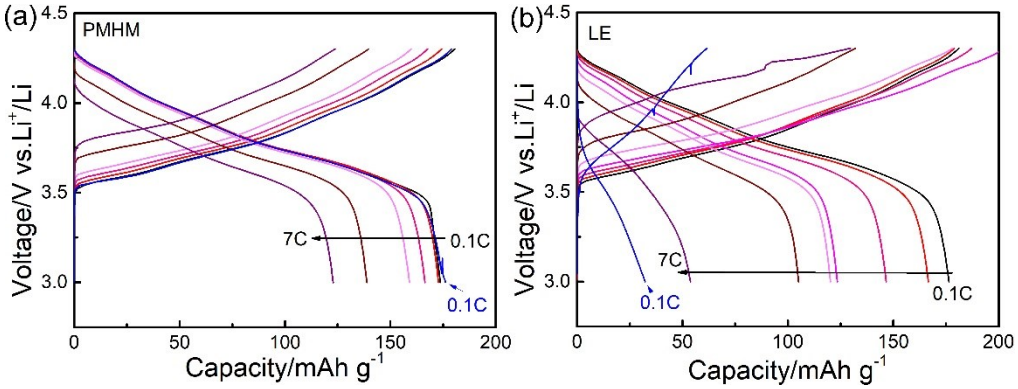

Fig. S15 Galvanostatic charge/discharge profiles of (a) NCA/PMHM/Li and (b) NCA/LE/Li batteries at varied current densities from 0.1 to 7C and return to 0.1C.

Charge/discharge profiles of NCA/PMHM/Li and NCA/LE/Li batteries at varied current densities are displayed in **Fig. S15**. NCA/PMHM/Li battery shows higher discharge capacity than NCA/LE/Li battery at higher rate. The superior rate performance of NCA/PMHM/Li battery is closely related to the improved interfacial compatibility between electrode and electrolyte.

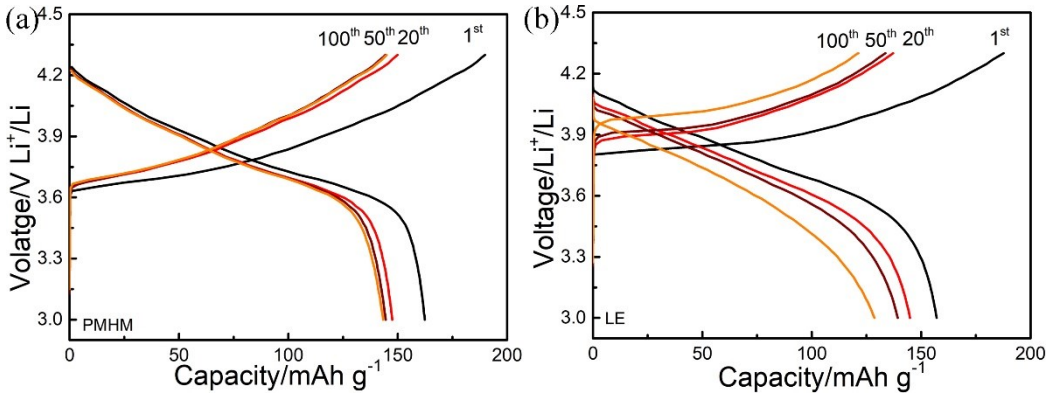

Fig. S16 Galvanostatic charge/discharge profiles of (a) NCA/PMHM/Li and (b) NCA/LE/Li batteries at 0.2C and 0°C.

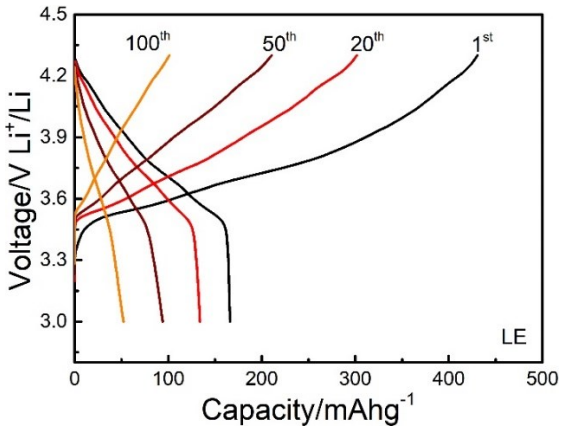

Fig. S17 Galvanostatic charge/discharge profiles of NCA/LE/Li batteries at at 0.2C and 60°C.

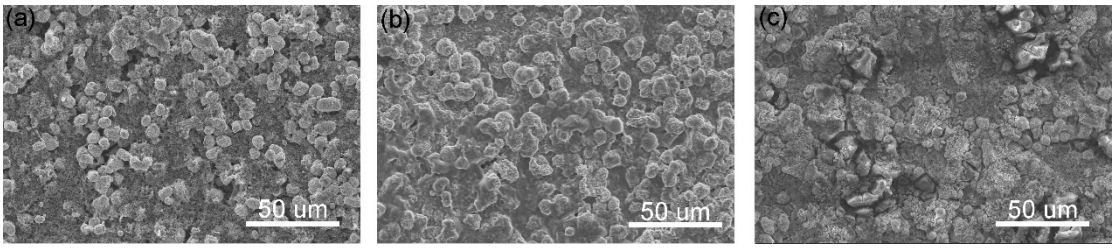

Fig. S18 Typical SEM images of NCA cathode at pristine (a) and cycled state assembled with (b) PMHM and (c) LE.

SEM images of NCA cathodes at pristine and cycled state assembled with PMHM and LE are displayed in **Fig. S18**. After cycling, NCA cathode assembled with PMHM presents a smooth and homogeneous surface. As a contrast, there are numerous clusters and cracks appeared on the surface of NCA cathode assembled with LE, suggesting the severe destruction of cathode structure.

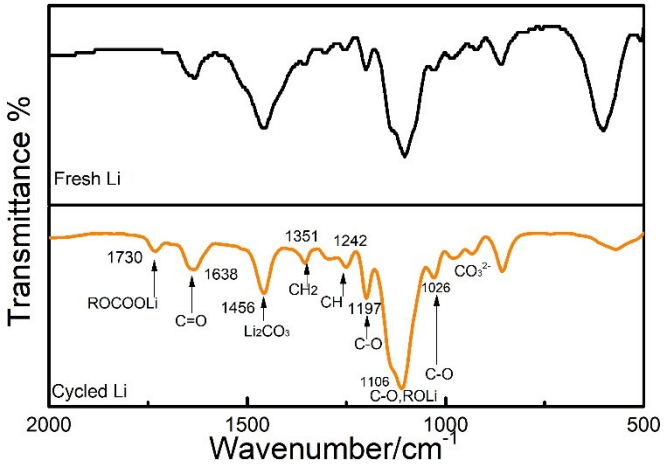

Fig. S19 FTIR spectra of fresh lithium foil and lithium-metal anode disassembled from NCA/PMHM/Li battery after cycling.

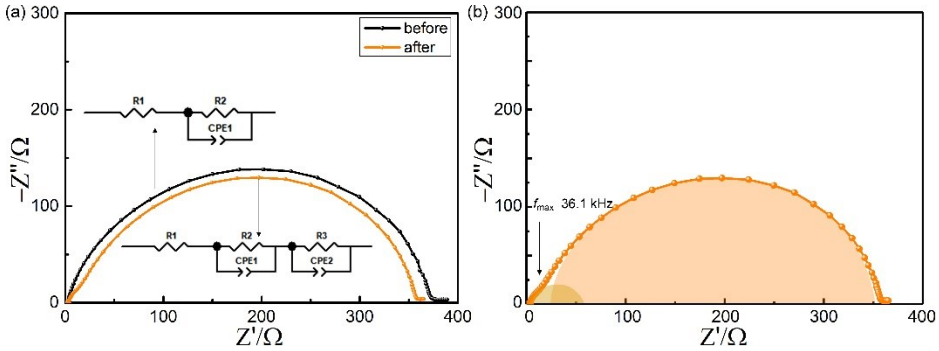

Fig. S20 (a) Nyquist spectra of the Li/Li symmetric cell assembled with PMHM (a) before and after the first cycle under a current density of 1 mA cm^{-2}. (b) Corresponding enlarged view and data fitting of cycled impedance spectra.

The ionic conductivity of SEI played a vital role in the electrochemical performance. Herein, the EIS of Li/PMHM/Li symmetric cell is conducted before and after 1 cycle to investigate the ionic conductivity of SEI. The initial impedance value is 370 Ω, which is mainly associated with the electrolyte resistance and charge transfer resistance.[4-5] The total impedance decreases after cycling, which may be attributed to the enlarged surface area of lithium anode after plating.[6] It is worth noting that a new semicircle appears at high frequency, which represents the effect caused by SEI layer and has been extensively researched.[7] The maximum frequency (f_{max}) of the newly-generated semicircle can be marked (31.6 kHz). The ionic conductivity of the SEI layer can be calculated according to the following equation [6, 8-10]

$$\sigma=2\pi f_{max}\varepsilon_0\varepsilon_r \quad (5)$$

where σ is the ionic conductivity of SEI, ε_0 (8.9×10^{-12} F m^{-1}) is the permittivity of free space and ε_r (10.0 F m^{-1}) is the permittivity of SEI layer. [10-11] Therefore, the ionic conductivity of SEI layer in Li/Li symmetrical cell is 0.17×10^{-4} S cm^{-1}.

Table S1 Electrochemical performances of NCA LMBs assembled with gel electrolytes in previous reports.

Polymer	Method	Voltage	Cathode	Cycles	Retention	Ref.
PVEC	In-situ	2.75-4.3V	NCA	200	0.5C,57.8%	[12]
PEGMEA	In-situ	2.6-4.3V	NCA	200	0.5C, 88%	[13]
Poly(allyl ether)	Casting	2.7-4.3V	NCA	100	0.1C, 95%	[14]
PETEA	In-situ	2.75-4.50V	NCA	200	5C, 92.5%	[15]
PEGDA	UV-cured	2.5-4.15V	NCA	100	0.11C, 77%	[16]
PEGDMA	UV-cured	3.0-4.25V	NCA	100	0.5C,92.2%	[17]
PCL		3.0-4.2V	$Li_{0.3}$NCA	80	1/6C, 80%	[18]
Poly ILs	Casting	2.5-4.5V	NCA	50	0.05, 88%	[19]
SA-PHC	electrospinning	3.0-4.3V	NCA	300	0.5C,68.3%	[20]

Table S2. Binding energy and peak assignment of C1s.

Binding energy (eV)	Peak assignment
284.6	C-H, C-C
285.6-285.8	C-O
286.4-286.8	C=O
288-290	O-C=O
291-292	Li_2CO_3, C-F from PVDF

Table S3. Binding energy and peak assignment of O1s.

Binding energy (eV)	Peak assignment
529.5	Metal-O
530.4-531	C=O, O-C=O, Li_2CO_3
532.4-532.9	C-O

Table S4. Binding energy and peak assignment of F1s.

Binding energy (eV)	Peak assignment
685.5-686.5	LiF, $LiPO_yF_z$, Li_xPF_y
687.9-688.1	C-F

Reference

[1] F. D. Han, A. S. Westover, J. Yue, X. L. Fan, F. Wang, M. F. Chi, D. N. Leonard, N. J. Dudney, H. Wang and C. S. Wang, *Nat. Energy*, 2019, **4**, 187-196.

[2] C. J. Hu, Y. B. Shen, M. Shen, X. Liu, H. W. Chen, C. H. Liu, T. Kang, F. Jin, L. Li, J. Li, Y. Q. Li, N. Zhao, X. X. Guo, W. Lu, B. W. Hu and L. W. Chen. *J. Am. Chem. Soc*., 2020, **142**, 8035-18041.

[3] Y. R. Su, J. Falgenhauer, A. Polity, T. Leichtweiß, A. Kronenberger, J. Obel, S. Q. Zhou, D. Schlettwein, J. Janek and B. K. Meyer, *Solid State Ionics*, 2015, **282**, 63-69.

[4] H. Y. Qiu, X. F. Du, J. W. Zhao, Y. T. Wang, J. W Ju, Z. Chen, Z. L. Hu, D. P. Yan, X. H. Zhou and G. L. Cui, *Nat. Chem.*, 2019, **10**, 5374.

[5] J. H. Yoo, W. K. Shin, S. M. Koo and D. W. Kim, *J. Power Sources*, 2015, **295**, 149-155.

[6] Z. L. Hu, S. Zhang, S. M. Dong, Q. Li, G. L. Cui and L. Q. Chen, *Chem. Mater.*, 2018, **30**, 4039-4047.

[7] M. R. Busche, T. Drossel, T. Leichtweiss, D. A. Weber, M. Falk, M. Schneider, M. L. Reich, H. Sommer, P. Adelhelm and J. Janek, *Nat. Chem.*, 2016, **8**, 426-434.

[8] P. Bruce and F. Krok, *Electrochim. Acta*, 1988, **33**, 1669-1674.

[9] S. E. Sloop and M. M. Lerner, *J. Electrochem. Soc*., 1996, **143**, 1292-1297.

[10] R. Bouchet, S. Lascaud and M. Rosso, *J. Electrochem. Soc*., 2003, **150**, A1385-A1389.

[11] K. A. Murugesamoorthi and J. R. Owen, *Br. Polym. J.*, 1988, **20**, 227-231.

[12] Z. Y. Lin, X. W. Guo, Z. C. Wang, B. Y. Wang, S. M. He, L. A. O'Dell, J. Huang, H. Li, H. J. Yu and L. Q. Chen, *Nano Energy*, 2020, **73**, 104786.

[13] R. Xu, X. Q. Zhang, X. B. Cheng, H. J. Peng, C. Z. Zhao, C. Yan and J. Q. Huang, *Adv. Funct. Mater*., 2018, **1705838**.

[14] V. Vijayakumar, D. Diddens, A. Heuer, S. Kurungot, M. Winter and J. R. Nair, *ACS Appl. Mater. Interfaces*, 2020, **12**, 567-579.

[15] X. L. Li, K. Qian, Y. B. He, C. Liu, D. C. An, Y. Y. Li, D. Zhou, Z. Q. Lin, B. H. Li, Q. H. Yang and F. Y. Kang, *J. Mater. Chem. A*, 2017, **5**, 18888-18895.

[16] W. F. Liang, Y. F. Shao, Y. M. Chen and Y. Zhu, *ACS Appl. Energy Mater.*, 2018, **1**, 6064-6071.

[17] Z. Y. Wei, Z. H. Zhang, S. J. Chen, Z. H. Wang, X. Y. Yao, Y. H. Deng and X. X. Xu, *Energy Storage Mater*., 2019, **22**, 337-345.

[18] M. M. Besli, C. Usubelli, M. Metzger, S. Hellstrom, S. Sainio, D. Nordlund, J. Christensen, G. Schneider, M. M. Doeff and S. Kuppan, *J. Mater. Chem. A,* 2019, **7**, 27135-27147.

[19] X. Wang, G. M. A. Girard, H. Zhu, R. Yunis, D. R. MacFarlane, D. Mecerreyes, A. J. Bhattacharyya, P. C. Howlett and M. Forsyth, *ACS Appl. Energy Mater*., 2019, **2**, 6237-6245.
[20] Y. Y. Sun, Y. Y. Wang, G. R. Li, S. Liu and X. P. Gao, *ACS Appl. Mater. Interfaces*, 2019, **11**, 14830-14839.